# Trailing-edge flap flow control for dynamic stall

**R. B. Green** **E. A. Gillies** **Y. Wang**
**richard.green@glasgow.ac.uk**
Department of Aerospace Engineering
University of Glasgow
Glasgow
UK

## ABSTRACT

Results of a series of oscillatory dynamic stall tests of a rotor aerofoil fitted with a pulsed, trailing-edge flap are presented. Flap deflection amplitude, motion profile, duration and starting phase were investigated to assess the potential of the flap for mitigating the adverse effects of dynamic stall, which is one of the limiting factors for rotor blades on the retreating side of a helicopter rotor. The tests were a continuation of the investigations by Ref. 1 who used a computational fluid dynamics method on a symmetric NACA section, and our results broadly confirm their conclusions by experimental test, using a modern rotor section. The results presented in this paper also confirm the observations from experimental work by Refs 2 and 3, which were undertaken at lower Reynolds number and with a larger flap. In the present study, the flap mitigates the high negative pitching moment and negative pitch damping seen in dynamic stall by strong suction being generated over the aerofoil lower surface, and it is the modification to the lower surface shape by the flap that creates this effect. The dynamic stall vortex acts to enhance the lower surface suction, and careful flap phasing and flap motion profile shaping can make the control more effective.

## NOMENCLATURE

| | |
|---|---|
| $a_2$ | two-dimensional aerodynamic cycle pitch damping coefficient |
| $a_{2n}$ | pitch damping coefficient calculated from normalised pitching moment |
| $a_{2nc}$ | contribution to $a_{2n}$ due to clockwise portion of $C_m$ loop |
| $c$ | aerofoil model chord, (m) |
| $C_d$ | aerofoil drag coefficient (due to pressure) |
| $C_m$ | pitching moment coefficient about aerofoil quarter chord |
| $C_n$ | aerofoil normal force coefficient |
| $C_p$ | pressure coefficient |
| $C_w$ | work coefficient |
| $f$ | aerofoil pitch oscillation frequency, (Hz) |
| $f_f$ | flap pitch oscillation frequency, (Hz) |
| $k$ | aerofoil pitch oscillation reduced frequency, $2\pi fc/2U_\infty$ |
| $t$ | time, (s) |
| $t_s$ | flap actuation start time, (s) |
| $T$ | aerofoil pitch oscillation period, (s) |
| $U_\infty$ | wind-tunnel speed, $ms^{-1}$ |
| $x$ | chordwise position on aerofoil, (m) |
| $\alpha$ | aerofoil angle-of-attack, (degrees) |
| $\hat{\alpha}$ | aerofoil pitch oscillation amplitude, (degrees) or (radians) |
| $\bar{\alpha}$ | mean aerofoil pitch angle, (degrees) |
| $\delta_f$ | flap pitch angle, (degrees) |
| $\psi$ | rotor azimuth angle, (degrees) |

## 1.0 INTRODUCTION

Dynamic stall on a helicopter rotor may occur over the retreating blades during high-speed forward flight and in manouevres under high load factor. Figure 1 shows how in forward flight there is an imbalance in dynamic pressure on either side of the rotor disk; to avoid a rolling moment on the aircraft lift is balanced by varying the blade pitch cyclically, with a high blade pitch angle on the retreating

**Paper No. 3604**. Manuscript received 24 April 2010, revised version received 22 October 2010, accepted 22 March 2011.

https://doi.org/10.1017/S0001924000006138 Published online by Cambridge University Press

side of the disk, and a low pitch angle on the advancing side. This cyclic pitching is combined with other unsteady effects such as blade flapping such that the aerodynamic angle-of-attack varies in an oscillating manner around the rotor azimuth. Dynamic stall effects on the retreating side, or transonic effects on the advancing side, are limiting factors in forward flight speed for the conventional helicopter, as they both introduce large pitching moments. During the dynamic stall process, blade flow separation is delayed to high angle-of-attack compared to stall in steady flow, but the sudden onset of flow separation typically results in the formation of a powerful, large scale vortex that convects along the chord over the aerofoil upper surface towards the trailing-edge. While the delay in stall produces enhanced lift, the stall itself results in high pitching moment excursions that may over-load control linkages and cause high levels of vibration. Furthermore stall flutter may arise from negative pitch damping. Thus, while much effort has been made to understand and characterise dynamic stall, and progress has been made in the design of aerofoils with good performance for dynamic stall, the phenomenon remains a limiting factor in helicopter performance.

McCroskey provides a useful review of dynamic stall. Light stall occurs when there is only a slight excursion beyond the static stall angle, and the thickness of the viscous layer is limited to a zone of the order of the aerofoil thickness. While there is loss of lift, increase in drag and a nose-down pitching moment in a similar manner to static stall, there is hysteresis in the airloads and a tendency towards negative pitch damping. It is well known in this stall regime that the basic flow separation behaviour is closely linked to the usually expected boundary layer separation behaviour (leading-edge or trailing-edge stall), and the stall behaviour depends on many factors including aerofoil shape, motion parameters and free stream Mach number. In deep stall the excursion beyond the static stall angle is far greater and the thickness of the region affected by viscosity is of the order of the aerofoil chord. The sequencing of events in dynamic stall has been described by Ref. 5 among others, and Fig. 2 shows a typical sequence of events. As the aerofoil passes the static stall angle[(1)] the boundary layer may remain thin but flow reversal may also take place within the boundary layer. Lift continues to increase at almost the same rate and the moment coefficient hardly changes. At a high enough angle-of-attack[(2)] moment stall occurs as the dynamic stall vortex begins to form in the leading-edge region. The formation and convection of this vortex towards the trailing-edge maintains and even increases the lift, while the pitching moment continues to fall rapidly. As the vortex passes the trailing-edge[(3)] lift stall occurs and the flow is fully separated. As the aerofoil angle-of-attack reduces the flow eventually becomes reattached, and the cycle is repeated. The moment coefficient schematic plot in Fig. 2 has been sketched to deliberately include a moment hysteresis loop; any clockwise portion of the loop produces a negative pitch damping contribution.

While the above descriptions outline the sequence of events, the fluid dynamic mechanisms active in dynamic stall remain obscure. Many earlier descriptions of dynamic stall hinted at the significance of the role of reversed flow penetrating upstream from the trailing-edge. However, subsequent analysis and experimentation showed that the critical events took place in the leading-edge region where pressure gradients, and hence vorticity production rates, are particularly intense. Reference 6 provide a review of these postulations. The basic processes occur within a small area of the boundary layer in the leading-edge area, and the rates of growth of the vortex structures are enormous. High resolution Particle Image Velocimetry at low chord Reynolds number (5,000) by Ref. 7 highlighted the interactions between closely neighbouring regions of positive and negative vorticity bearing fluid in the leading-edge area, and the experiments seem to support the theoretical propositions. Practical dynamic stall on rotorcraft, however, occurs at far higher Reynolds numbers and hence experimentation at the required scale within the very thin boundary layer would be very challenging indeed. Additionally compressibility effects need to be considered, as shock wave formation and the influence of density change on vorticity production itself become important. All the above aspects present additional challenges for CFD simulations of dynamic stall. Much effort has been made in the design of aerofoil sections that give good performance before the occurrence of dynamic stall restricts the flight envelope of a helicopter, but design efforts must concentrate on the leading-edge area where the dynamic stall vortex springs from without adversely affecting the transonic performance of the blade at the advancing side.

Further extending the useful operating envelope of a rotor may be possible through the use of leading-edge slats (see, for example Refs 8 and 9), and higher harmonic control shows promise Ref. 10), but there are also prospects from the correct application of a flow control technology applied on the blade. An obvious strategy is to devise a scheme that further delays stall onset, by modifying the flow at the leading-edge, and there have been a number of studies to demonstrate its feasibility. The study reported in Ref. 8 addresses this using a variable shape leading-edge in compressible dynamic stall, and this is an interesting candidate approach. However, the leading-edge environment on a rotor is severe, as evidenced by the use of erosion strips along most operational rotors, and flow control actuation in this region may be difficult to engineer. An alternative application of flow control is to alleviate the adverse effects of dynamic stall once it has occurred; if the large pitching moment deviations could be attenuated and the tendency towards negative pitch damping could be removed without significant loss of lift, then an extension of the flight envelope could be achieved. Various studies have shown that this is possible using a trailing-edge flap pitched to coincide with the dynamic stall. This scheme was proposed and theoretically investigated using CFD by Ref. 1, who observed that a phased, upwards pitching of the trailing-edge flap restored positive pitch damping compared to the negative pitch damping in the base case. A key feature of the control scheme was that the flap was pitched during only a short period of the aerofoil oscillation cycle (a pulsed flap), and that at all other times the flap deflection relative to the aerofoil chord line was zero. Numerous other researchers have since investigated this trailing-edge flap control scheme. Most notably Refs 2 and 3 show results that confirm the effectiveness of the technique proposed by 1, and they conclude that the useful aerodynamic effect of the flap in reducing the pitching moment excursion is the generation of suction over the aerofoil lower surface.

The current paper extends the study of Ref. 1 with a series of wind-tunnel tests on a modern operational rotor section at typical operational Reynolds number. For a typical dynamic stall case that involves negative pitch damping, it is shown that an appropriately phased flap actuation will restore the positive pitch damping, reduce the pitching moment overshoot and yet retain the majority of the desirable lift increment. The experimental tests were done at a significantly higher Reynolds number compared to Refs 2 and 3, used an aerofoil section representative of those used on a practical helicopter and used a much smaller flap. The major conclusions serve to underline the performance benefits that may be gained from the use of a trailing-edge flap, especially one of much smaller size.

## 2.0 EXPERIMENTAL METHOD

An aerofoil model was constructed based on the coordinates of a modern, operational rotor section. Company confidentiality prevents revealing further details of the section, other than it has moderate camber, with a good dynamic stall performance, typical of several other modern blade lifting sections. Its chord length was $c = 0{\cdot}5$m, and it spanned the shorter dimension of the Glasgow University 1·52m × 1·78m 'Handley Page' closed-return, low-speed wind-tunnel. End plates were used to isolate end effects, giving an effective span of 1·1m. The aerofoil was pitched around its quarter chord using a linear hydraulic actuator and crank mechanism, and this was programmed to

https://doi.org/10.1017/S0001924000006138 Published online by Cambridge University Press

execute sinusoidal pitch profiles $\alpha(t) = \bar{\alpha} + \hat{\alpha}\mathrm{Sin}(2\pi ft)$ with variable mean angle $\bar{\alpha}$ and amplitude $\hat{\alpha}$ up to a frequency $f$ of 5Hz. A linear angular displacement transducer was used to provide feedback for the aerofoil actuation system. The model was equipped with a trailing-edge flap of 15% aerofoil chord length spanning between the end plates. A diagram of the aerofoil/flap junction is shown in Fig. 3. The flap was made by cutting off the aft 15% of the aerofoil and mounting it onto a hinge, and a circular recess was formed in the main body of the aerofoil for the hinge to sit in. The bearing surfaces were lined with a hard-wearing material so that the flap could move freely with no airflow through the junction area. Flap pitch motion control was provided by a STA2510 servo-tube actuator (a linear motor) made by Copley motion systems. The excellent dynamic response of this motor allowed rapid, pulsed-profile, pitching motions of the flap to be executed in a variety of pitch profiles (e.g. sinusoidal, pitch-up, hold, pitch-down), with flap pitch amplitudes $\delta_f$ in excess of 20° at frequencies typically up to $f_f$ = 10Hz. The flap could be phased to execute its pulsed pitch profile at any point during the aerofoil pitch cycle, and a separate angular displacement transducer provided the angular position of the flap relative to the model. A schematic diagram of the aerofoil and flap are shown in Fig. 4; the sense of the flap deflection $\delta_f$ is shown in frame (a) of the figure, and a typical sinusoidal flap deflection profile is shown in frame (b). The flap actuation starts at time $t_s$ after the aerofoil passes through the mean angle $\bar{\alpha}$ on the upstroke. Representative rotor azimuth positions $\psi$ are also shown on the figure, and the retreating side of the disk is from $\psi$ = 180° to $\psi$ = 360°. The primary instrumentation for the aerofoil model consisted of 39 surface mounted pressure transducers arranged in a chordwise fashion at the mid-span of the model, with 23 on the upper surface and the remainder on the lower surface. Chordwise pressure transducer positions are shown in Table 1 The wind-tunnel speed was set at speed $U_\infty$ = 30ms$^{-1}$ to give a nominal test Reynolds number of 1 million and Mach number around 0·1. Tests were run with the aerofoil model performing a sinusiodal pitch profile at reduced frequency $k = 2\pi fc/2U_\infty$ up to 0·15 and $\bar{\alpha}$ and $\hat{\alpha}$ up to 20° and 8° respectively. Flap deflection phasing, duration, amplitude and motion profile (sinusoidal, trapezoidal) were investigated for cases with the aerofoil in deep stall.

Data acquisition was performed by a PC interfaced to Bakker Electronics BE256 12-bit Analogue to Digital converter modules. The system conducted automatic offset removal and gain adjustment to optimise resolution. Pressure transducer data were sampled simultaneously at up to 50kHz per channel using a multi-channel data capture system. During an aerofoil oscillatory test the aerofoil was set in motion for six oscillation cycles before the data sampling was performed. Data were sampled over four cycles and were then averaged based on phase. Other data such as aerofoil and flap pitch angle, wind-tunnel dynamic pressure, air temperature, barometric pressure were also sampled by the data acquisition system. On the basis of pressure transducer non-linearity (0·2%) and calibration errors, data acquisition system resolution and dynamic pressure measurement accuracy, the uncertainty in the derived pressure coefficient was estimated to be 0·5%. The uncertainty in instantaneous aerofoil and flap incidence was 0·25 degrees.

## 3.0 DATA ANALYSIS

For analysis of the results it is important that the effectiveness of the flap is demonstrated. The two-dimensional aerodynamic cycle pitch damping coefficient $a_2$ is given by;

$$a_2 = -C_w/\pi\hat{\alpha}^2,$$

**Table 1**
**Chordwise co-ordinates of pressure transducers. Transducers 1 to 6 on the upper surface and 34 to 39 on the lower surface are mounted on the pitching flap**

| Transducer number | *x/c* | surface | transducer number | *x/c* | surface |
|---|---|---|---|---|---|
| 1 | 0·993 | upper | 25 | 0·001 | lower |
| 2 | 0·972 | upper | 26 | 0·007 | lower |
| 3 | 0·952 | upper | 27 | 0·020 | lower |
| 4 | 0·930 | upper | 28 | 0·050 | lower |
| 5 | 0·896 | upper | 29 | 0·100 | lower |
| 6 | 0·874 | upper | 30 | 0·200 | lower |
| 7 | 0·820 | upper | 31 | 0·400 | lower |
| 8 | 0·740 | upper | 32 | 0·650 | lower |
| 9 | 0·660 | upper | 33 | 0·800 | lower |
| 10 | 0·580 | upper | 34 | 0·874 | lower |
| 11 | 0·500 | upper | 35 | 0·896 | lower |
| 12 | 0·420 | upper | 36 | 0·930 | lower |
| 13 | 0·340 | upper | 37 | 0·952 | lower |
| 14 | 0·270 | upper | 38 | 0·972 | lower |
| 15 | 0·200 | upper | 39 | 0·993 | lower |
| 16 | 0·140 | upper | – | – | – |
| 17 | 0·100 | upper | – | – | – |
| 18 | 0·075 | upper | – | – | – |
| 19 | 0·050 | upper | – | – | – |
| 20 | 0·025 | upper | – | – | – |
| 21 | 0·010 | upper | – | – | – |
| 22 | 0·003 | upper | – | – | – |
| 23 | 0·001 | upper | – | – | – |
| 24 | 0·000 | leading-edge | – | – | – |

https://doi.org/10.1017/S0001924000006138 Published online by Cambridge University Press

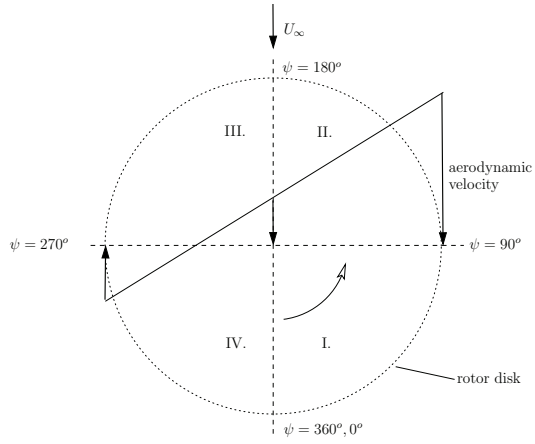



Figure 1. Rotor azimuth $\psi$, forward flight speed $U_\infty$ and aerodynamic velocity on the blade. There is reduced dynamic pressure over the retreating side of the disk (quadrants III and IV), and dynamic stall tends to occur between quadrants III and IV.

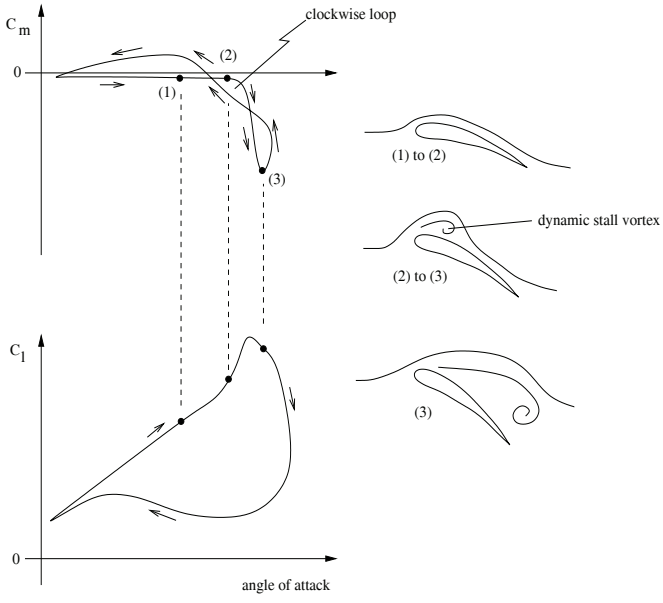



Figure 2. Schematic diagram showing the notional phasing of events in deep dynamic stall.

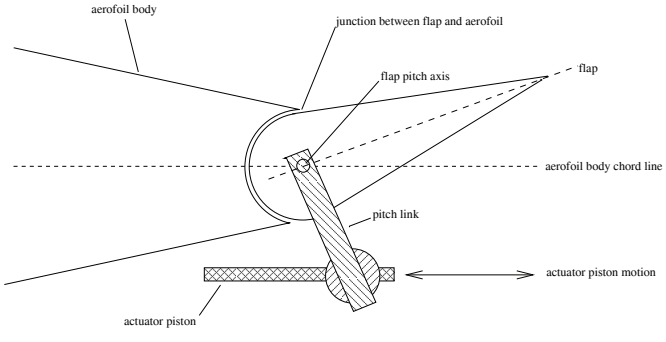



Figure 3. Diagram showing the aerofoil body/ flap joint. The surfaces either side of the junction were lined with a hard-wearing material to allow smooth rotation of the flap with no air flow through the junction. Flap pitching is provided through the pitch link by the actuator piston motion.

where the aerofoil oscillation amplitude $\hat{\alpha}$ expressed in radians, $C_w$ is the work coefficient

$$C_w = \oint C_m(\alpha) d\alpha,$$

and $C_m$ is the pitching moment coefficient of the aerofoil about the quarter chord point of the aerofoil (positive nose up).

Additional theoretical details regarding the above are described in Ref. 11. Negative damping for a rotor blade implies the air flow is doing work on the blade, and a negatively damped blade will suffer an exponential growth in its amplitude of oscillation if the structural dynamics permit. On a rotor, excursions into dynamic stall are encountered on the retreating blade under certain conditions of high forward speed, and negative damping on the stall cycle is clearly undesirable. The results to be presented also include the contribution $a_{2c}$ to $a_2$ a due to the clockwise portion of the $C_m$ loop (see Fig. 2), and the normal force coefficient $C_n$, the coefficient of force acting normal to the chord line of the aerofoil.

## 4.0 RESULTS AND DISCUSSION

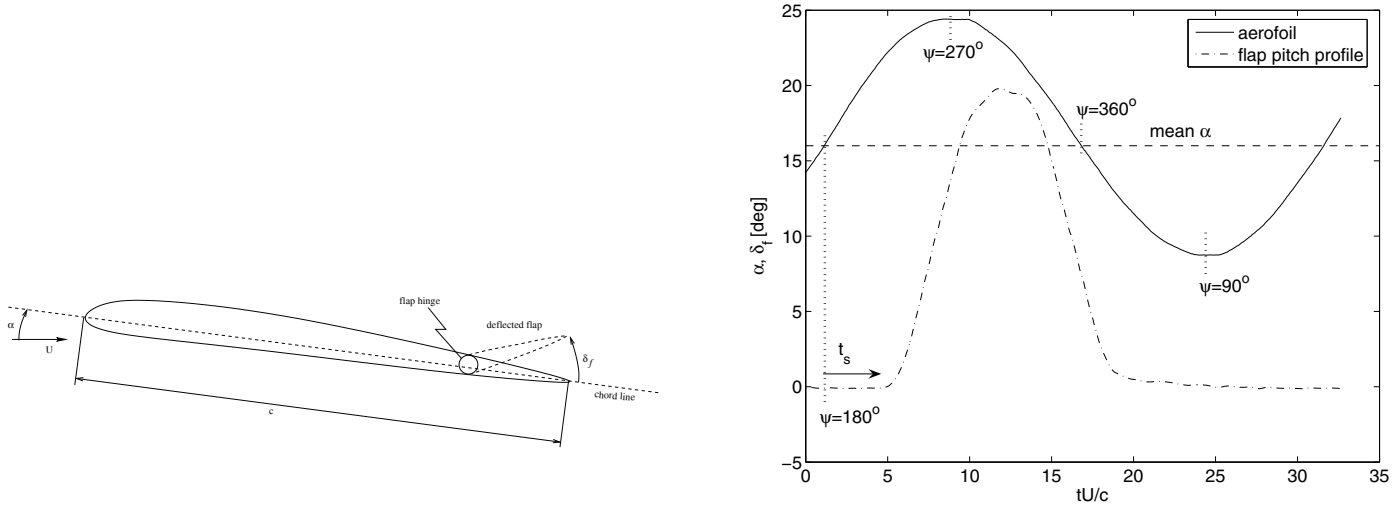
This section presents a description and discussion of the phenomena observed, followed by an investigation of the various flap actuation parameters on dynamic stall. Aerodynamic coefficient data are presented in a normalised fashion due to commercial confidentiality. $C_m$ and $C_n$ data are normalised with their respective maximum magnitude values for the reference (base) case with no flap deflection. Pressure coefficient $C_p$ plots are presented normalised to the maximum $-C_p$ for the reference case with no flap deflection.

### 4.1 Baseline dynamic stall case

Results for a deep dynamic stall case at $k = 1{\cdot}102$, $\bar{\alpha} = 16°$ and $\hat{\alpha} = 8°$ are presented in Fig. 5. $C_m$, shown in frame (a), remains relatively constant during the pitch up until around 22° when $C_m$ falls rapidly, and this is due to the dynamic stall process leading to the collapse of leading-edge suction and subsequent low pressure over the aft section of the aerofoil due to the dynamic stall vortex. As the aerofoil pitches back down to low $\alpha$ the moment response begins to form a clockwise loop. The further reduction in $C_m$ as the aerofoil pitches down through 23° is due to the passage of the dynamic stall vortex over the trailing-edge and the subsequent shedding of a secondary vortex. As the aerofoil continues its downstroke through 18 and the flow becomes reattached the moment response forms an anti-clockwise loop. Clockwise loops on the moment history are responsible for generating negative pitch damping. The overall normalised cycle pitch damping coefficient is $a_{2n} = -0{\cdot}061$, and the contribution to this from the clockwise portion of the $C_m$ loop is $a_{2nc} = -0{\cdot}427$. If the maximum angle-of-attack of the aerofoil can be considered as when a rotor blade is at the $\psi = 270°$ azimuth position, then as a simple illustrative model this suggests that the portion of the azimuth affected by the negatively damped clockwise loop is from $\psi = 192°$ to $\psi = 348°$. The normal force in frame (b) of Fig. 5 shows a typical dynamic stall response, with a significant lift overshoot compared to the static test, and a brief lift increase due to the dynamic stall vortex as the aerofoil approaches the maximum incidence. The rapid collapse of lift occurs on the downstroke as the vortex approaches the aerofoil trailing-edge. There is a brief lift recovery during the aerofoil downstroke due to the aforementioned vortex shedding, and attached flow behaviour is established towards the end of the downstroke.

The upper surface pressure distribution for this case is shown in Fig. 6 frame(a). The leading-edge is at the top of each figure, time runs from left to right and aerofoil angle-of-attack and effective rotor azimuth position are indicated. The pressure is normalised to the minimum $C_p$, and selected $-C_p$ contours are shown. The build up of leading-edge suction and its collapse just prior to the

https://doi.org/10.1017/S0001924000006138 Published online by Cambridge University Press




(a ) aerofoil and flap

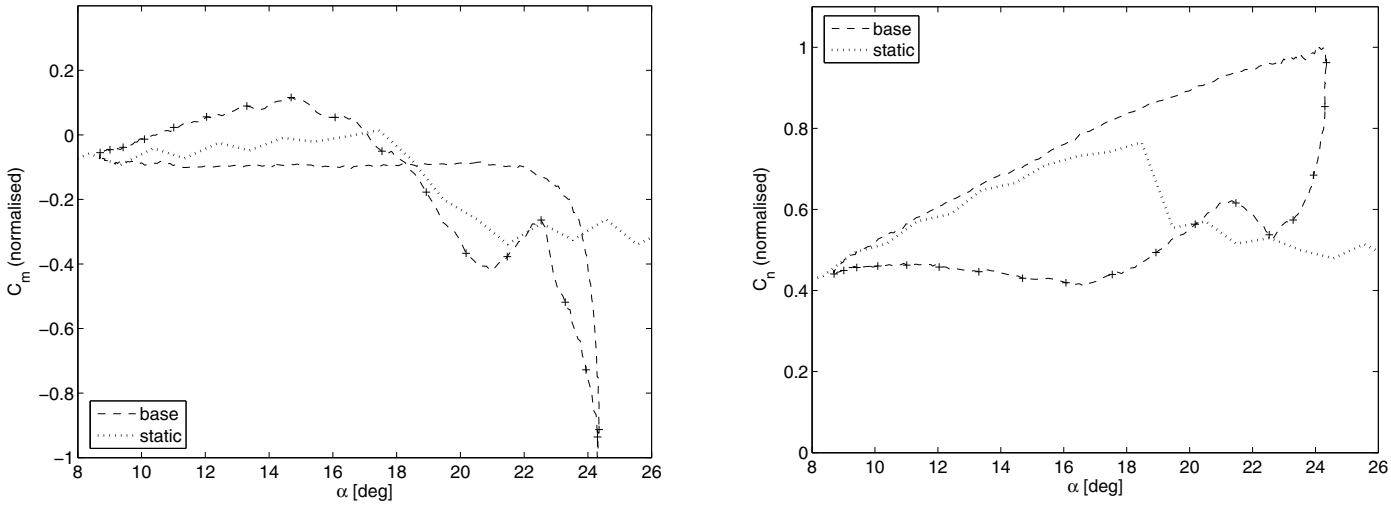
(b) aerofoil and flap pitch profile

Figure 4. Aerofoil and flap deflection angles. The sense of the positive flap deflection angle $\delta_f$ is shown in frame (a). Frame (b) shows a typical aerofoil angle $\alpha$ and flap angle $\delta_f$ history for a sinusoidal profile; the mean aerofoil angle is indicated, and the flap actuation starts at time $t_s$ from the start of the aerofoil oscillation cycle as it pitches up through the mean angle-of-attack $\alpha$. Representative rotor azimuth positions $\psi$ are shown. Aerofoil and flap actuation parameters are $k$ = 0·102, $\bar{\alpha}$ = 16°, $\hat{\alpha}$ = 8°. Flap actuation parameters are a sinusoidal actuation profile, start time of $t_s/T$ = 1/9 at $\bar{\alpha}$ = 21·8° upstroke, $\delta_f$ = 20°, flap actuation duration $T/2$.

maximum angle-of-attack at $\alpha$ = 24° are clear. Progress of the dynamic stall vortex is shown by the suction ridge springing from the collapse in leading-edge suction and travelling to the trailing-edge from around the $x/c$ = 0·25 location, and it is highlighted on frame (a) by the dashed line. Note a much weaker suction ridge travelling along the chord after the main suction ridge; this is a secondary vortex (trailing-edge vortex), which has been reported previously by various researchers. Ref. 12 showed results of flow visualisation and attributed the formation of the trailing-edge vortex to the action of the dynamic stall vortex as it passed over the trailing-edge. Lower surface pressure data, Fig. 6 frame (b), indicate positive pressure over the bulk of the aerofoil oscillation cycle apart from a very small suction zone at the trailing-edge which develops as the dynamic stall vortex is seen to approach and cross the trailing-edge upper surface. The major suction peak on the lower surface in the trailing-edge region just after maximum angle-of-attack coincides with the passage of the dynamic stall vortex over the trailing-edge upper surface.

### 4.2 Description of effect of flap actuation

Pitching moment and normal force coefficient histories for a sample flap controlled case are shown in Fig. 7; the baseline dynamic stall case with no flap actuation is as described above for Fig. 5. The flap deflection amplitude is $\delta_f$ = 20° upwards, it is actuated at a delay of $t_s/T$ = 1/9 into the aerofoil oscillation cycle as indicated on the figure, and the flap actuation duration is $T/2$. (Note the flap and aerofoil pitch profiles are the same as in Fig. 4(b)). The minimum $|C_m|$ is reduced by one third compared to the base case, but a larger positive

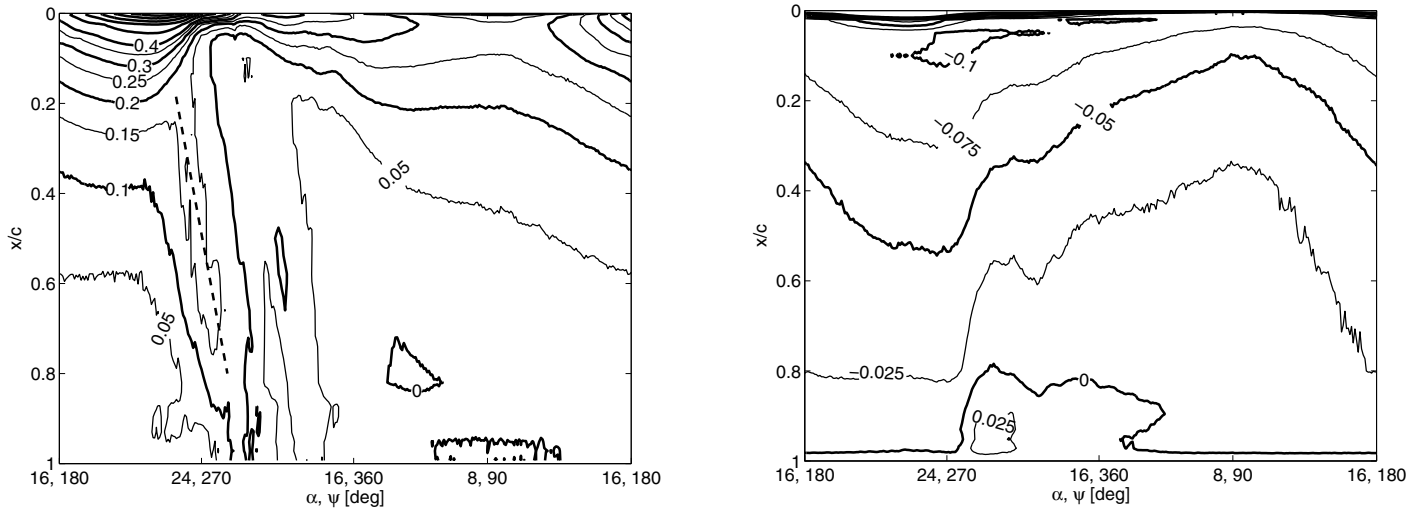



(a) pitching moment coefficient

(b) normal force coefficient

Figure 5. Baseline dynamic stall case for $k$ = 0·102, $\bar{\alpha}$ = 16°, $\hat{\alpha}$ = 8° showing pitching moment and normal force coefficient behaviour over the pitch cycle. Results for static (non-pitching) tests are shown by the dotted line. Data are normalised to maximum magnitude $C_m$ and $C_n$. The '+' symbols on the plots indicate the aerofoil downstroke phase of the dynamic test.

https://doi.org/10.1017/S0001924000006138 Published online by Cambridge University Press



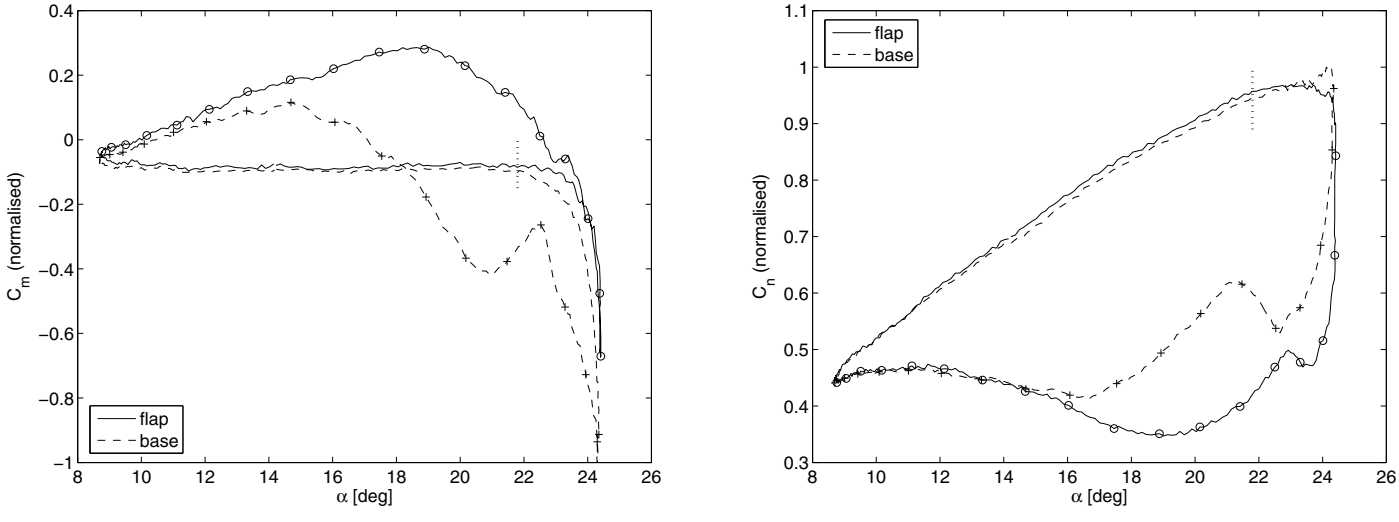

(a) upper surface

(b) lower surface

Figure 6. Upper and lower surface pressure distributions ($-C_p$) for baseline dynamic stall test for case shown in Fig. 5, $k$ = 0·102, $\bar{\alpha}$ = 16°, $\hat{\alpha}$ = 8°. The aerofoil leading-edge is at the top of the picture, time runs from left to right, and the aerofoil angle-of-attack $\alpha$ and effective rotor azimuth $\psi$ are shown. levels normalised to maximum $-C_p$ are shown. In the upper surface plot the thick contour lines are separated by intervals of 0·1 with the thin lines at intermediate values, and the contours are labelled to a maximum value of 0·4. The dashed line running along the ridge around contour level 0·15 indicates the passage of the dynamic stall vortex. For the lower surface plot the thick contour levels are separated by 0·05 with thin lines at intermediate values shown.

$C_m$ is reached on the downstroke. Note that at the start of the aerofoil downstroke the flap is already at an angle of $\delta_f$ = 12° and is pitching upwards. The clockwise moment loop formed during the initial phase of the downstroke on the base case is completely absent, and the damping in the clockwise loop in this case is $a_{2n_c}$ =–0·001. The portion of the azimuth affected by the clockwise loop is from $\psi$ = 246° to $\psi$ = 294°, but the damping is so small that the range may be considered as irrelevant. As the downstroke progresses the moment forms a large, anti-clockwise loop, giving a normalised cycle pitch damping of $a_{2n}$ = 0·987; the flap is therefore highly effective in almost removing the clockwise moment loop and producing a positively damped response compared to the case with no flap deflection for which $a_{2n}$ = –0·061. The maximum $C_n$, on the other hand, is almost unchanged, but on the downstroke the reduction in $C_n$ is larger compared to the base case and the fluctuations in $C_n$ are smaller.

Upper and lower surface pressure data are shown in Fig. 8, and the flap actuation phases are indicated on each frame. When compared to the pressure from the unactuated case shown in Fig. 6, the major features of the pressure distribution are still present. Peak suction on the dynamic-stall vortex suction ridge on the upper surface, frame (a), is slightly reduced, and the only significant effect of the flap appears to be on the secondary vortex, where no clear upper surface suction signature of the trailing-edge vortex is visible. The absence of the footprint of this trailing-edge vortex in the flap actuated case here is notable, and the further effect of flap actuation on the trailing-edge vortex effect will be discussed later. The pressure distribution over the aerofoil lower surface, frame (b), shows that the effect of the flap

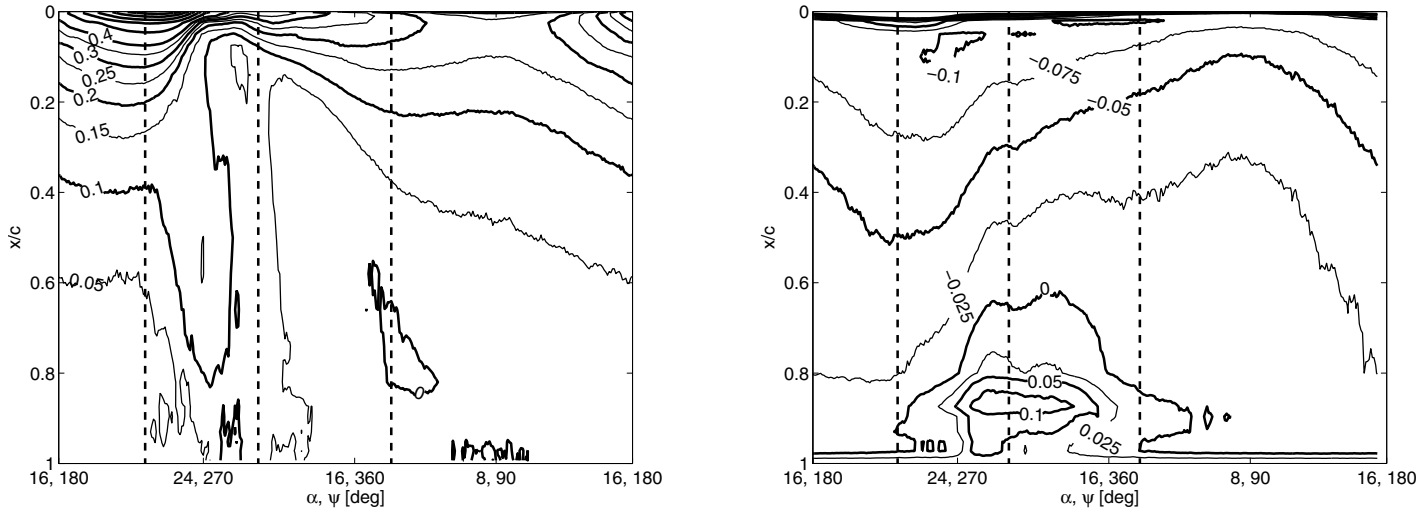



(a) pitching moment coefficient

(b) normal force coefficient

Figure 7. Effect of flap actuation on dynamic stall for $k$ = 0·102, $\bar{\alpha}$ = 16°, $\hat{\alpha}$ = 8°. Flap actuation parameters are a sinusoidal actuation profile, start time of $t_s/T$ = 1/9 at a = 21·8° upstroke, $\delta_f$ = 20°, flap actuation duration $T/2$. Data are normalised to maximum magnitude $C_m$ and $C_n$. In each frame the flap-actuated case is represented by the solid line and the reference base dynamic stall case (no flap actuation) by the dashed line. The 'o' and '+' symbols on the plots indicate the aerofoil downstroke phases of the respective dynamic stall tests. The flap actuation start time is indicated by the vertical, dashed line crossing the upstroke data at $\alpha$ = 21·8°.

https://doi.org/10.1017/S0001924000006138 Published online by Cambridge University Press

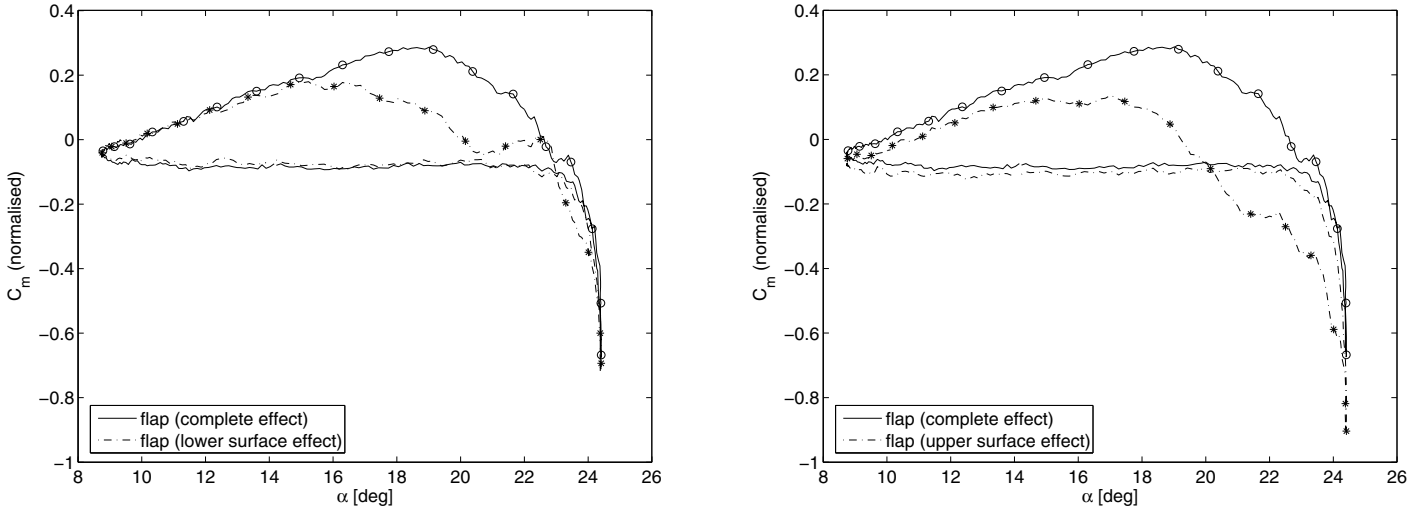



(a) lower surface effect (b) upper surface effect

Figure 8. Upper and lower surface pressure distributions ($-C_p$) for dynamic stall tests with flap actuation for case shown in Fig. 7: $k$ = 0·102, $\bar{\alpha}$ = 16°, $\hat{\alpha}$ = 8°; flap actuation parameters are a sinusoidal actuation profile, start time of $t_s/T$ = 1/9 at $\alpha$ = 21·8° upstroke, $\delta_f$ = 20°, flap actuation duration $T/2$. The aerofoil leading-edge is at the top of the picture, time runs from left to right, and the aerofoil angle-of-attack $\alpha$ and effective rotor azimuth $\psi$ are shown. $-C_p$ levels normalised to maximum $-C_p$ for the base case with no flap deflection are shown. In the upper surface plot the thick contour lines are separated by intervals of 0·1 with the thin lines at intermediate values, and the contours are labelled to a maximum value of 0·4. For the lower surface plot the thick contour levels are separated by 0·05 with thin lines at intermediate values shown. The black, dashed lines on both frames indicate start of flap actuation (left), flap maximum angle (middle), end of flap actuation (right)

deflection is the generation of relatively high suction over a large length of the aft portion of the aerofoil lower surface both ahead of and behind the aerofoil/flap-hinge interface at the $x/c$ = 0·85 location (thus confirming the observations due to Ref. 2). As soon as the flap starts to deflect, the suction pressure increases aft of the $x/c$ = 0·85 location, and at higher flap angles suction is observed as far forward as the $x/c$ = 0·6 location. This may be complared to the baseline case with no flap deflection, Fig. 6 frame (b), which shows a brief, weak suction pulse around the lower surface trailing-edge area as the dynamic stall vortex passes the trailing-edge.

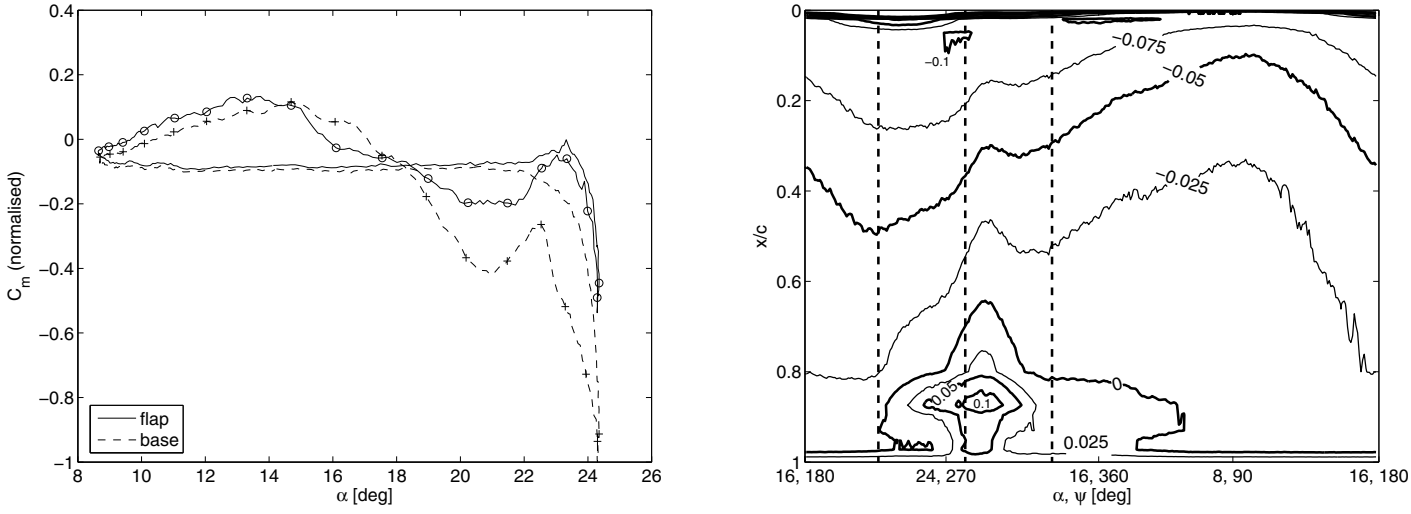
In Ref. 2 it was concluded that it was the suction effect over the lower surface that was primarily responsible for the significant effects of the pitching flap on the $C_m$ behaviour. It is therefore instructive to investigate the relative importance of the upper and lower surface pressure distributions on the pitching moment cycle for the actuated flap case. The individual contributions of the upper surface and lower surface pressure modifications towards the effectiveness of the flow control can be assessed as follows: to isolate the upper surface effect, the pressure data from the upper surface during an actuated cycle is combined with data from the lower surface during an unactuated cycle; to isolate the lower surface effect, the pressure data from the lower surface during an actuated cycle is combined with data from the upper surface during an unactuated cycle. Figure 9 shows the results of this analysis, and the plot




(a) lower surface effect (b) upper surface effect

Figure 9. Illustration of effects of flap actuated upper and lower surface aerofoil pressure distributions on $C_m$ (normalised). Dynamic stall test is the flap actuated case shown in Fig. 7 for $k$ = 0·102, $\bar{\alpha}$ = 16°, $\hat{\alpha}$ = 8°. Flap parameters are a sinusoidal profile with start time $t_s/T$ = 1/9, flap duration $T/2$ and amplitude 20°. The symbols on the plots indicate the downstroke phase of the aerofoil oscillation. In each frame the moment has been calculated from a combination of the pressure data from one surface for the base case (no flap deflection) and the other surface with the flap deflection.

https://doi.org/10.1017/S0001924000006138 Published online by Cambridge University Press




(a) pitching moment coefficient

(b) lower surface pressure distribution

Figure 10. Effect of flap actuation on dynamic stall for $k = 0{\cdot}102$, $\bar{\alpha} = 16°$, $\hat{\alpha} = 8°$. Flap parameters are a sinusoidal profile with start time $t_s/T = 1/9$, flap duration of $T/3$ and amplitude 20°, and normalised $C_m$ (frame (a)) and pressure distribution ($-C_p$) over the lower surface (frame (b)) are shown. The symbols on the frame (a) indicate the downstroke phase of the aerofoil oscillation. For the pressure distribution plot in frame (b) the leading-edge is at the top of the figure and time runs from left to right. $-C_p$ levels normalised to maximum $-C_p$ for the base case are shown, and the thick contour levels are separated by 0·05 with thin lines at intermediate values shown. The black, dashed lines are start of flap actuation (left), flap maximum angle (middle), end of flap actuation (right).

**Table 2**
**Effect of flap duration period on dynamic stall for $k = 0{\cdot}102$, $\bar{\alpha} = 16°$, $\hat{\alpha} = 8°$; sinusoidal flap profile; $t_s/T = 1/9$; $\delta_f = 20°$. All coefficients are normalised. The table lists damping coefficients, azimuth range for the clockwise $C_m$ loop and $C_m$ and $C_n$ values**

| flap deflection duration ($T$) | $a_{2n}$ | $a_{2nc}$ | *Clockwise* $C_m$ *loop* $\psi$ (deg) | $C_{m_{min}}$ | $C_{n_{max}}$ | $C_{n_{max}}$ |
|---|---|---|---|---|---|---|
| no flap | –0·061 | –0·427 | 192 to 348 | 1 | 1 | 0·411 |
| 1/3 | 0·206 | –0·142 | 194 to 346 | 0·537 | 0·940 | 0·402 |
| 1/2 | 0·987 | –0·001 | 246 to 294 | 0·674 | 0·969 | 0·347 |

shows $C_m$ from the actuated case and $C_m$ from the combined actuated/unactuated data. The lower surface pressure effect alone (frame (a)) almost completely removes the anti-clockwise part of the moment loop from the base case and the normalised damping coefficient is $a_{2n} = 0{\cdot}594$, while the upper surface pressure effect (frame (b)) reduces the size of the anti-clockwise moment loop such that the damping becomes positive with $a_{2n} = 0{\cdot}350$. The increased suction over the lower surface rather than the slight loss in suction over the upper surface is responsible for the loss of lift on the aerofoil downstroke. The lower surface suction effect is therefore dominant,

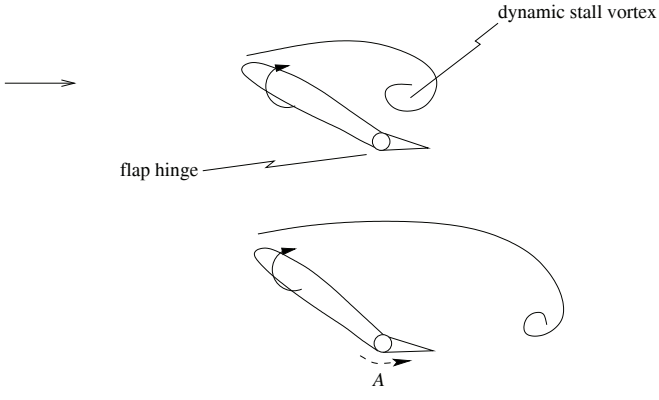



Figure 11. Acceleration of flow $A$ over lower surface of flap hinge by induction effect of stall vortex as it passes aerofoil trailing-edge.

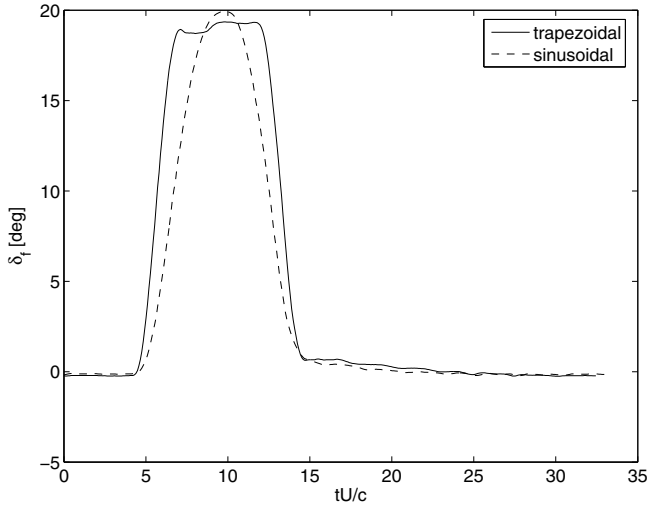
and this analysis supports the conclusion of Ref. 2, but it is remarked that the suction effect on the lower surface appears quite far ahead of the flap.

### 4.3 Flap actuation duration

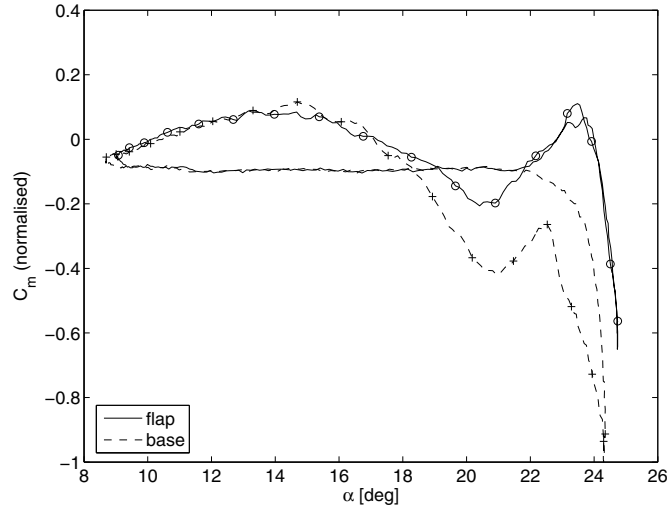
The useful effect of the flap on the cycle pitch damping is further illustrated by examining the influence of the duration of the flap actuation. Figure 10 shows $C_m$ and the lower surface pressure distribution for a shorter flap actuation duration of $T/3$, with the remaining aerofoil and flap parameters being the same as the case discussed above in Figures 7 and 8 ($k = 0{\cdot}102$; $\bar{\alpha} = 16$; $\hat{\alpha} = 8$; sinusoidal profile, $t_s/T = 1/9$; $\delta_f = 20°$).

Frame (a) on Fig. 10 shows that the minimum $C_m$ is not as low as for the longer flap duration case described in Fig. 7, and there are large fluctuations on the aerofoil downstroke. The size of the anticlockwise and clockwise segments of the $C_m$ loop are both diminished compared to the base dynamic stall case, with the normalised cycle damping coefficient positive at $a_{2n} = 0{\cdot}206$, and the clockwise loop damping at $a_{2nC} = -0{\cdot}142$. The pressure distribution shows that the lower surface suction is still increasing even as the flap is pitching back towards zero deflection, and the upper surface pressure distribution (not shown) shows that the dynamic stall vortex (peak suction) is at around the $x/c = 0{\cdot}8$ location when the flap is at maximum $\delta_f$. On the other hand in the longer flap duration case described previously, Fig. 8, the stall vortex had already passed over the trailing-edge and peak suction around the lower surface of the flap hinge was attained before the flap reached maximum deflection. The dynamic stall vortex will induce a high velocity flow over the aft portion of the lower surface of the aerofoil (lower surface suction

https://doi.org/10.1017/S0001924000006138 Published online by Cambridge University Press




(a) flap pitch profiles




(a) $C_m$

Figure 12. Effect of trapezoidal flap actuation on dynamic stall for $k$ = 0·102, $\bar{\alpha}$ = 16°, $\hat{\alpha}$ = 8°. Trapezoidal flap profile and normalised $C_m$ response are shown. Flap parameters are a trapezoidal profile with start time $t_s/T$ = 1/9, flap duration $T$/3 and amplitude 20°. An equivalent sinusoidal flap profile is shown in frame (a) for comparison, and the symbols on the frame (b) indicate the downstroke phase of the aerofoil oscillation.

**Table 3**
**Effect of flap deflection amplitude on dynamic stall for $k$ = 0·102, $\bar{\alpha}$ = 16°, $\hat{\alpha}$ = 8° sinusoidal flap profile; $t_s/T$ = 1/9; duration $T$/3. All coefficients are normalised. The table lists damping coefficients, azimuth range for the clockwise $C_m$ loop and $C_m$ and $C_n$ values**

| of(deg)z | $a_{2n}$ | $a_{2nc}$ | *Clockwise $C_m$ loop $\psi$* (deg) | $C_{m_{min}}$ | $C_{n_{max}}$ | $C_{n_{max}}$ |
|---|---|---|---|---|---|---|
| no flap | –0·061 | –0·427 | 192 to 348 | 1 | 1 | 0·411 |
| 10 | 0·13 | –0·252 | 194 to 346 | 0·793 | 0·961 | 0·425 |
| 15 | 0·298 | –0·146 | 200 to 340 | 0·656 | 0·949 | 0·438 |
| 20 | 0·206 | –0·142 | 194 to 346 | 0·537 | 0·940 | 0·402 |

associated with the stall vortex is present in the undeflected flap case), and if the flap still has a significant deflection it is plausible that there will be higher velocity flow around the lower surface flap hinge. This is depicted in Fig. 11, where flow $A$ is accelerated around the flap hinge due to the velocity induction effect of the stall vortex. As a consequence for the shorter flap duration the minimum $C_m$ is not as low as in the longer flap duration case, but the useful lower surface suction effect is lost more quickly as the stall vortex still exerts a strong suction effect on the upper surface, and this explains the large fluctuations in $C_m$. Another effect seen on the upper surface is that the suction pressures ($-C_p$) along the stall vortex induced suction ridge are not as high as in the longer flap duration case, which suggests that the stall vortex has been deflected slightly away from the aerofoil surface by the flap reaching a higher angle sooner in the vortex convection phase.

A summary of the effect of flap actuation duration on the important aerodynamic parameters is shown in Table 2. Both flap durations provide positive damping with a large reduction in the minimum $C_m$ at the expense of some loss of lift. The longer duration flap reduces the area of the clockwise $C_m$ loop to almost zero (almost neutral damping over that phase), and the azimuthal duration is considerably shorter.

### 4.4 Flap amplitude

Flap amplitude was investigated for the basic dynamic stall reference case at $k$ = 0·102; $\hat{\alpha}$ = 16°; $\bar{\alpha}$ = 8° with flap duration $T$/3 and flap phasing $t_s/T$ = 1/9 for a sinusoidal actuation profile. Table 3 shows a summary of the important aerodynamic parameters. All flap cases provide positive damping, but the $\delta_f$ = 15° case provides the

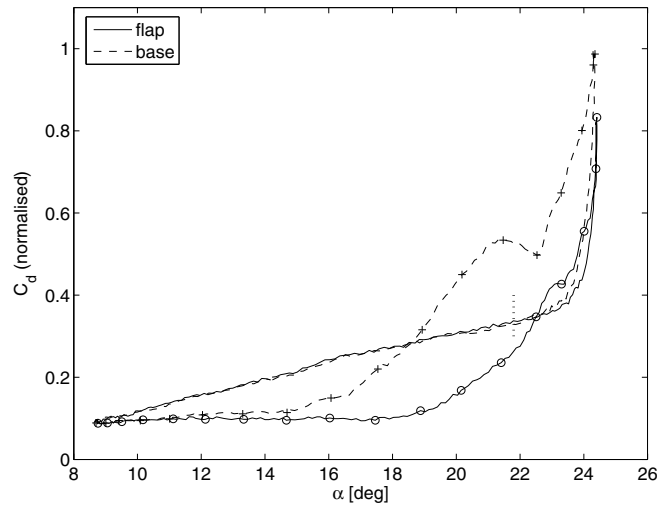



Figure 13. Effect of flap actuation on pressure drag coefficient during dynamic stall for $k$ = 0·102, $\bar{\alpha}$ = 16°, $\hat{\alpha}$ = 8°. Flap actuation parameters are a sinusoidal actuation profile, start time of $t_s/T$ = 1/9 at $\alpha$ = 21·8° upstroke, $\delta_f$ = 20°, flap actuation duration $T$/2. Data are normalised to maximum $C_d$ (drag due to pressure only). In each frame the flap-actuated case is represented by the solid line and the reference base dynamic stall case (no flap actuation) by the dashed line. The 'o' and '+' symbols on the plots indicate the aerofoil downstroke phases of the respective dynamic stall tests. The flap actuation start time is indicated by the vertical, dashed line crossing the upstroke data at $\alpha$ = 21·8°.

https://doi.org/10.1017/S0001924000006138 Published online by Cambridge University Press

**Table 4**
**Effect of flap actuation deflection profile (`sine' for sinusoidal and 'trap' for trapezoidal) and amplitude on dynamic stall for $k$ = 0·102, $\bar{\alpha}$ = 16°, $\hat{\alpha}$ = 8°; flap start time $t_s/T$ = 1/9; flap duration $T$/3. All coefficients are normalised. The table lists damping coefficients, azimuth range for the clockwise $C_m$ loop and $C_m$ and $C_n$ values**

| flap profile | $\delta_f$(deg) | $a_{2n}$ | $a_{2nc}$ | *Clockwise $C_m$ loop* $\psi$ (deg) | $C_{m_{min}}$ | $C_{n_{max}}$ | $C_{n_{max}}$ |
|---|---|---|---|---|---|---|---|
| no flap | – | –0·061 | –0·427 | 192 to 348 | 1 | 1 | 0·411 |
| sine | 10 | 0·13 | –0·252 | 194 to 346 | 0·793 | 0·961 | 0·425 |
| sine | 15 | 0·298 | –0·146 | 200 to 340 | 0·656 | 0·949 | 0·438 |
| sine | 20 | 0·206 | –0·142 | 194 to 346 | 0·537 | 0·940 | 0·402 |
| trap | 10 | 0·339 | –0·166 | 206 to 334 | 0·778 | 0·987 | 0·447 |
| trap | 15 | 0·470 | –0·047 | 207 to 333 | 0·704 | 0·945 | 0·418 |
| trap | 20 | 0·303 | –0·051 | 196 to 343 | 0·651 | 0·948 | 0·433 |

highest damping with a still respectable minimum moment and lift performance.

### 4.5 Flap amplitude and actuation profile

The flap could be programmed to execute a range of motion types. A pitch-up, hold, pitch-down (trapezoidal) profile was executed, and a typical profile for a flap deflection amplitude $\delta_f$ = 20° and duration $T$/3 is shown in Fig. 12 (a sinusoidal actuation profile is shown for comparison). $C_m$ is shown in frame (b) of this figure for the dynamic stall case $k$ = 0·102; $\hat{\alpha}$ = 16°; $\bar{\alpha}$ = 8° with the flap actuation starting at $t_s/T$ = 1/9. The flap reaches maximum deflection more quickly than in the sinusoidal actuation case, giving higher suction earlier on over the lower surface flap-hinge area, and this causes the moment to become more positive during the aerofoil upstroke. Cases with a later flap deflection show a lower moment increase as the dynamic stall process proceeds over the upper surface. The trapezoidal actuation shares many features with the sinusoidal actuation shown in Fig. 10, frame(a); a clockwise loop is present on the $C_m$ cycle, and a large portion of the $C_m$ loop is neutrally damped. Table 4 shows a summary of results showing the effect of flap pitch amplitude for a set of sinusoidal and trapezoidal flap tests. Both actuation profiles are effective in producing positive cycle damping, but the trapezoidal cases in particular have the added benefit of more positive cycle damping and greater reduction of the negative damping in the clockwise portion of the $C_m$ loop.

### 4.6 Effect of flap actuation duration for trapezoidal profile

Table 5 shows the effect of shortening the flap duration length for the trapezoidal actuation. The flap is effective in producing positive damping for all cases except the $T$/5 duration, which is worse than the no flap case. The overall dynamic stall period is around 0·133$T$ in duration, so a slightly later phasing for the duration flap may produce a better response. However such fine phasing of the flap may not be practical for a real-world application of the device as reliability issues might become significant. Examination of the negative damping $a_{2nC}$ suggests that a shorter flap duration is even less effective, and in all but the longest flap duration the extent of azimuth affected by negative or neutral damping is relatively unaffected by the flap.

### 4.7 Flap phasing

Different flap start times $t_s$ were investigated for the trapezoidal motion profile with flap duration $T$/3 and amplitude 20°, and results are shown in Table 6. In the later actuation case at $t_s/T$ = 1/8 the stall process is already well underway and the stall vortex is approaching the mid-chord by the time the flap has reached maximum deflection. In this case the upper surface suction pressures associated with the footprint of the dynamic stall vortex are also higher, particularly around the trailing-edge. On the other hand, in the earliest actuation case, the flap has reached maximum deflection before the vortex has progressed beyond $x/c$ = 0·2 and suction pressures are lower along the chord. As with the motion profile effect, this suggests that the higher flap deflection angle earlier in the dynamic stall sequence leads to the stall vortex following a trajectory slightly further away from the aerofoil surface. The later actuation case at $t_s/T$ = 1/8 also has a stronger suction over the lower surface aerofoil-flap hinge compared to the earlier actuation at $t_s/T$ = 1/10, suggesting stronger vortex induced suction in this case. The clockwise $C_m$ loop is almost completely absent on the $t_s/T$ = 1/8 case. The flap phasing does not have a strong effect on the overall cycle damping for this motion profile and actuation duration, but as mentioned earlier the flap actuation duration phasing may be of greater importance for short flap durations.

### 4.8 Analysis of cycle drag coefficient

The pressure measurement allows for the aerofoil drag due to pressure to be determined, and at those portions of the cycle where the flap is deployed this will comprise the majority of the drag owing to the gross flow separations that are present. Although the flap is not proposed as a device for alleviating drag, it is at least worth describing the effects on an estimation on drag in this paper. Figure 13 shows the effect of the flap on normalised $C_d$ for the dynamic stall case shown in Fig. 7, and it is seen that while there is no effect on the aerofoil upstroke the flapped case has lower drag on the downstroke. The pressure drag comprises resolved components of the aerofoil thrust and normal force coefficients, and the lower drag in the flap actuated case is predominantly due to the much lower normal force during the downstroke with the flap actuation.

**Table 5**
**Effect of flap deflection duration for trapezoidal flap profile on dynamic stall for $k$ = 0·102, $\bar{\alpha}$ = 16°, $\hat{\alpha}$ = 8°; flap start time $t_s/T$ = 1/9; $\delta_f$ = 20°. All coefficients are normalised. The table lists damping coefficients, azimuth range for the clockwise $C_m$ loop and $C_m$ and $C_n$ values**

| flap deflection duration ($T$) | $a_{2n}$ | $a_{2nc}$ | *Clockwise $C_m$ loop*$\psi$ (deg) | $C_{m_{min}}$ | $C_{n_{max}}$ | $C_{n_{min}}$ |
|---|---|---|---|---|---|---|
| no flap | –0·061 | –0·427 | 192 to 348 | 1 | 1 | 0·411 |
| 1/2 | 1.209 | –0·030 | 243 to 297 | 0·635 | 0·955 | 0·316 |
| 1/3 | 0·303 | –0·051 | 196 to 343 | 0·651 | 0·948 | 0·433 |
| 1/4 | 0·188 | –0·282 | 201 to 338 | 0·569 | 0·943 | 0·443 |
| 1/5 | –0·095 | –0·496 | 197 to 342 | 0·696 | 0·942 | 0·448 |

https://doi.org/10.1017/S0001924000006138 Published online by Cambridge University Press

**Table 6**
**Effect of flap start time on dynamic stall for $k = 0{\cdot}102$, $\bar{\alpha} = 16°$, $\hat{\alpha} = 8°$ flap duration $T/3$; $\delta_f = 20°$, trapezoidal flap pitch profile. All coefficients are normalised. The table lists damping coefficients, azimuth range for the clockwise $C_m$ loop and $C_m$ and $C_n$ values**

| flap start time($t_s/T$) | $a_{2n}$ | $a_{2nc}$ | *Clockwise* $C_m$ *loop* $\psi$ (deg) | $C_{m_{min}}$ | $C_{n_{max}}$ | $C_{n_{min}}$ |
|---|---|---|---|---|---|---|
| no flap | –0·061 | –0·427 | 192 to 348 | 1 | 1 | 0·411 |
| 1/10 | 0·415 | –0·064 | 206 to 334 | 0·692 | 0·931 | 0·441 |
| 1/9 | 0·303 | –0·051 | 196 to 343 | 0·651 | 0·948 | 0·433 |
| 1/8 | 0·426 | 0·0 | 193 to 347 | 0·603 | 0·950 | 0·424 |

## 5.0 CONCLUSIONS

A pitching, trailing-edge flap of 15% length has been shown to be effective in mitigating the adverse effects of dynamic stall. With appropriate flap phasing, duration and amplitude, positive pitch cycle damping could be achieved, and local negative damping regions in the moment loops were reduced in size. The beneficial effect of the flap is due to suction induced on the aerofoil-flap hinge area on the lower surface, thus confirming the conclusions of Refs 2 and 3, but different flap pitch profiles, phase and duration suggest the behaviour of the stall vortex over the upper surface is acting to enhance this mechanism. Tailoring the flap pitch profile may have benefits, but it is especially important that the flap reaches a high deflection angle quickly.

## ACKNOWLEDGEMENTS

The study used data originally collected under the United Kingdom Defence Aerospace Research Partnership but since analysed via independent means. The assistance of A. Brockehurst of AgustaWestland, Yeovil, England, is acknowledged. Contributors to the technical element of the work include Prof R. Galbraith, Prof F. Coton and the technical staff of the Department of Aerospace Engineering, University of Glasgow.

## REFERENCES

1. FESZTY, D., GILLIES, E.A. and VEZZA, M. Alleviation of airfoil dynamic stall moments via trailing-edge-flap flow control, *AIAA J*, 2004, **42**, (1), pp 17–25.
2. GERONTAKOS, P. and LEE, T. Dynamic stall flow control via a trailing-edge flap, *AIAA J*, 2006, **44**, (3), pp 469– 480.
3. LEE, T. and GERONTAKOS, P. Effect of flap motion on unsteady aerodynamic loads, *J Aircr*, 2007, **44**, (1), pp 334–338.
4. MCCROSKEY, W.J. Unsteady airfoils, *Annual Review of Fluid Mechanics*, 1982, **14**, pp 185–311.
5. CARR, L.W., MCALISTER, K.W. and MCCROSKEY, W.J. Analysis of the development of dynamic stall based on oscillating airfoil experiments. NASA TN D-8382, 1977.
6. DOLIGALSKI, T.L., SMITH, C.R. and WALKER, J.D.A. Vortex interactions with walls, *Annual Review of Fluid Mechanics*, 1994, **26**, pp 573–616.
7. SHIH, C., LOURENCO, L.M. and KROTHAPALLI, A. Investigation of flow at leading and trailing-edges of pitching-up airfoil, *AIAA J*, 1995, **33**, (8), pp 1369–1376.
8. CHANDRASEKHARA, M.S., WILDER, M.C. and CARR. L.W. Compressible dynamic stall control: comparison of two approaches, *J Aircr*, 2001, **38**, (3), pp 448–453.
9. YU, Y.H., LEE, S., MCALISTER, K.W., TUNG, C. and WANG. C.M. Dynamic stall control for advanced rotorcraft application, *AIAA J*, 1995, **33**, (2), pp 289–295.
10. NGUYEN, K. Active control of helicopter blade stall, *J Aircr*, 1998, **35**, (1), pp 91–98.
11. CARTA, F.O. An analysis of the stall flutter instability of helicopter rotor blades, *J American Helicopter Society*, 1967, **12**, (4), pp 1–18.
12. PANDA, J. and ZAMAN, K.B.M.Q. Experimental investigation of the flow field of an oscillating airfoil and estimation of lift from wake surveys. *J Fluid Mechanics*, 1994, (265), pp 65–95.

https://doi.org/10.1017/S0001924000006138 Published online by Cambridge University Press